JCI insight

RESEARCH ARTICLE

Lowering circulating apolipoprotein E levels improves aged bone fracture healing

Rong Huang,[1,2] Xiaohua Zong,[1,2] Puviindran Nadesan,[2] Janet L. Huebner,[1] Virginia B. Kraus,[1,2,3,4] James P. White,[1,4] Phillip J. White,[1,4] and Gurpreet S. Baht[1,2,3]

[1]Duke Molecular Physiology Institute, [2]Department of Orthopaedic Surgery, [3]Department of Pathology, and [4]Department of Medicine, Duke University, Durham, North Carolina, USA.

Age is a well-established risk factor for impaired bone fracture healing. Here, we identify a role for apolipoprotein E (ApoE) in age-associated impairment of bone fracture healing and osteoblast differentiation, and we investigate the mechanism by which ApoE alters these processes. We identified that, in both humans and mice, circulating ApoE levels increase with age. We assessed bone healing in WT and ApoE$^{-/-}$ mice after performing tibial fracture surgery: bone deposition was higher within fracture calluses from ApoE$^{-/-}$ mice. In vitro recombinant ApoE (rApoE) treatment of differentiating osteoblasts decreased cellular differentiation and matrix mineralization. Moreover, this rApoE treatment decreased osteoblast glycolytic activity while increasing lipid uptake and fatty acid oxidation. Using parabiosis models, we determined that circulating ApoE plays a strong inhibitory role in bone repair. Using an adeno-associated virus–based siRNA system, we decreased circulating ApoE levels in 24-month-old mice and demonstrated that, as a result, fracture calluses from these aged mice displayed enhanced bone deposition and mechanical strength. Our results demonstrate that circulating ApoE as an aging factor inhibits bone fracture healing by altering osteoblast metabolism, thereby identifying ApoE as a new therapeutic target for improving bone repair in the elderly.

Introduction

Bone fractures occur in 50% of the population, causing significant morbidity and mortality and costing the US health care system over $20 billion annually (1). Complications, such as nonunion or delayed union, occur in 5%–10% of fracture cases, and this rate is increased in the elderly population. Accordingly, more attention needs to be devoted toward understanding the molecular processes involved in fracture repair, particularly those that are altered with age. Development of therapies targeting these specific signaling molecules would therefore enhance bone healing in the geriatric population, decreasing secondary complications. Here, we investigate a protein, potentially novel to fracture repair, as one of these potential targets.

Bone healing is a complex and dynamic process involving numerous signaling molecules, pathways, and cell types in 4 stages: the inflammatory phase involving secretion of inflammatory markers, the formation of the cartilaginous or soft callus, the conversion of the fibrocartilaginous callus to the bony callus by osteoblasts, and finally the remodeling phase converting trabecular bone to compact bone (2, 3). Critical within fracture healing is the role of the osteoblast, the bone-forming cell. During fracture healing, osteoprogenitor cells differentiate to osteoblasts, and subsequently, during the bony callus formation, osteoblasts deposit a collagenous matrix and are responsible for matrix mineralization. Despite this critical role for osteoblasts in bone fracture healing, the molecular factors that influence osteoblast activation during bone repair are still being elucidated.

In our previous work investigating aged bone regeneration, we identified apolipoprotein E (ApoE) to be one of many candidates potentially involved in aged bone fracture healing (4). ApoE is a widely expressed lipoprotein classically associated with lipid metabolism and fatty acid transport (5–8). ApoE polymorphisms are present in 20% of the population and are associated with hypercholesterolemia, atherosclerosis (7, 9), and Alzheimer's disease (10–12). More recently, clinical evidence has revealed that these ApoE polymorphisms are also associated with decreased bone mineral density and increased risk of hip and vertebral fracture (13–16). Mouse models lacking ApoE expression display increased cortical thickness, trabecular number, and bone mineral density (14, 17). However, a role for ApoE in fracture healing and musculoskeletal aging remains to be investigated.

Conflict of interest: The authors have declared that no conflict of interest exists.

Submitted: March 27, 2019
Accepted: August 8, 2019
Published: September 19, 2019.

Reference information: *JCI Insight*. 2019;4(18):e129144. https://doi.org/10.1172/jci.insight.129144.

Here, we sought to understand the role of ApoE in age-associated deficiencies in bone fracture healing. Our previous work has established the importance of circulating factors in the age-associated impairment of bone regeneration. Here, we use our established tibial fracture model (18, 19) coupled with μCT and histological analysis as well as our parabiosis models to identify a role for circulating ApoE in bone fracture healing. We identify ApoE as a negative regulator of osteoblast differentiation and combine this work with functional metabolic assessment and transcript analysis to identify the mechanism by which ApoE influences osteoblast differentiation. Finally, we identify that lowering circulating ApoE levels, using siRNA strategies, in aged mouse models leads to improved bone fracture healing. Collectively, our findings demonstrate that ApoE impairs bone fracture healing in an age-dependent manner by decreasing osteoblast differentiation.

Results

Loss of ApoE increases bone deposition in the fracture callus. To determine whether ApoE plays a role in bone fracture healing, we conducted tibial fracture surgery, stabilizing the fractured tibia with an intramedullary pin, on 4-month-old WT ($ApoE^{+/+}$) and ApoE-knockout ($ApoE^{-/-}$) littermate mice. To account for the stages of bone healing, we assessed fracture calluses harvested at 7 days, 14 days, and 21 days after injury (Figure 1A) using a variety of methods, including analysis of inflammatory and angiogenic markers using ELISA, development of the cartilaginous callus using histological techniques, matrix mineralization using μCT, and bone deposition using calcein double labeling and histomorphometry.

Bony callus formation was investigated 21 days after injury using multiple analytical methods (Figure 1, A and B). μCT analysis showed that fracture calluses from $ApoE^{-/-}$ mice were of similar size as WT mice but contained more mineralized bone tissue than those from WT mice (Figure 1, C–E), and the tissue mineral density of deposited tissue was higher in $ApoE^{-/-}$ fracture calluses than in WT calluses (Figure 1F). Our histological analysis yielded concordant results. Histomorphometry of paraffin sections of decalcified fracture calluses stained with Alcian blue/hematoxylin/Orange G revealed significantly increased bone tissue deposition within $ApoE^{-/-}$ fracture calluses than within WT fracture calluses (Figure 1, G and H). To study bone formation and mineral apposition kinetics during repair, we used calcein double labeling, injecting the mice with calcein dye at 17 and 20 days after fracture, then harvested the calluses at 21 days after injury (Figure 1I). Using fluorescent imaging of nondecalcified sections, we measured the distance between the dye fronts because this represents bone accrual between the 2 calcein injections. Fracture calluses from $ApoE^{-/-}$ mice clearly displayed an increased mineral apposition rate (MAR, Figure 1J) and an increased bone formation rate/bone surface (BFR/BS, Figure 1K).

Inflammatory and angiogenic markers were measured after 7 days of healing. ELISA of specific markers in both serum and lysates from the local healing bone tissue (fracture callus) of WT and $ApoE^{-/-}$ mice revealed neither inflammatory nor angiogenic differences. IL-10, IL-1β, IL-6, KC, TNF-α, MCP-1, and MIP-1α were expressed at similar levels in both WT and $ApoE^{-/-}$ serum (Supplemental Figure 1A; supplemental material available online with this article; https://doi.org/10.1172/jci.insight.129144DS1). Likewise, angiogenic markers VEGF and VCAM-1 were present in similar quantities in WT and $ApoE^{-/-}$ serum and fracture calluses (Supplemental Figure 1, B and C).

To assess cartilaginous callus formation, fractured tibiae were harvested at 14 days after injury, fixed, decalcified, and paraffin embedded. Histomorphometry, performed on histological sections stained using Alcian blue/hematoxylin/Orange G, revealed no difference in the amount of cartilaginous tissue deposition (shown in blue) within the fracture callus of WT mice relative to $ApoE^{-/-}$ mice (Supplemental Figure 2, A and B).

Because ApoE has been linked to phagocytosis in muscle wound debridement (20), we investigated the potential effect of ApoE deletion on osteoclasts, multinucleated bone-resorbing cells. Tartrate-resistant acid phosphatase (TRAP) staining, performed on 21-day fracture calluses in $ApoE^{-/-}$ and WT mice (Supplemental Figure 3A), showed no differences in osteoclast activity or in osteoclast number (Supplemental Figure 3B), consistent with previous findings of Shilling et al., who investigated osteoclast activity during bone homeostasis in $ApoE^{-/-}$ mouse models (14).

Overall, these data indicate that ApoE deletion in mouse models improves bone fracture healing by increasing bone formation while leaving other aspects of repair unaffected.

Osteoblast differentiation and activity are decreased by rApoE treatment. The changes observed in fracture healing secondary to ApoE deletion occurred at 21 days after fracture, a time at which both bone formation and osteoblast activity are at their peak (3). To determine the role of ApoE in osteoblast differentiation and activity, we used a cell culture model for osteoblast differentiation. Bone marrow stromal cells aspirated from the

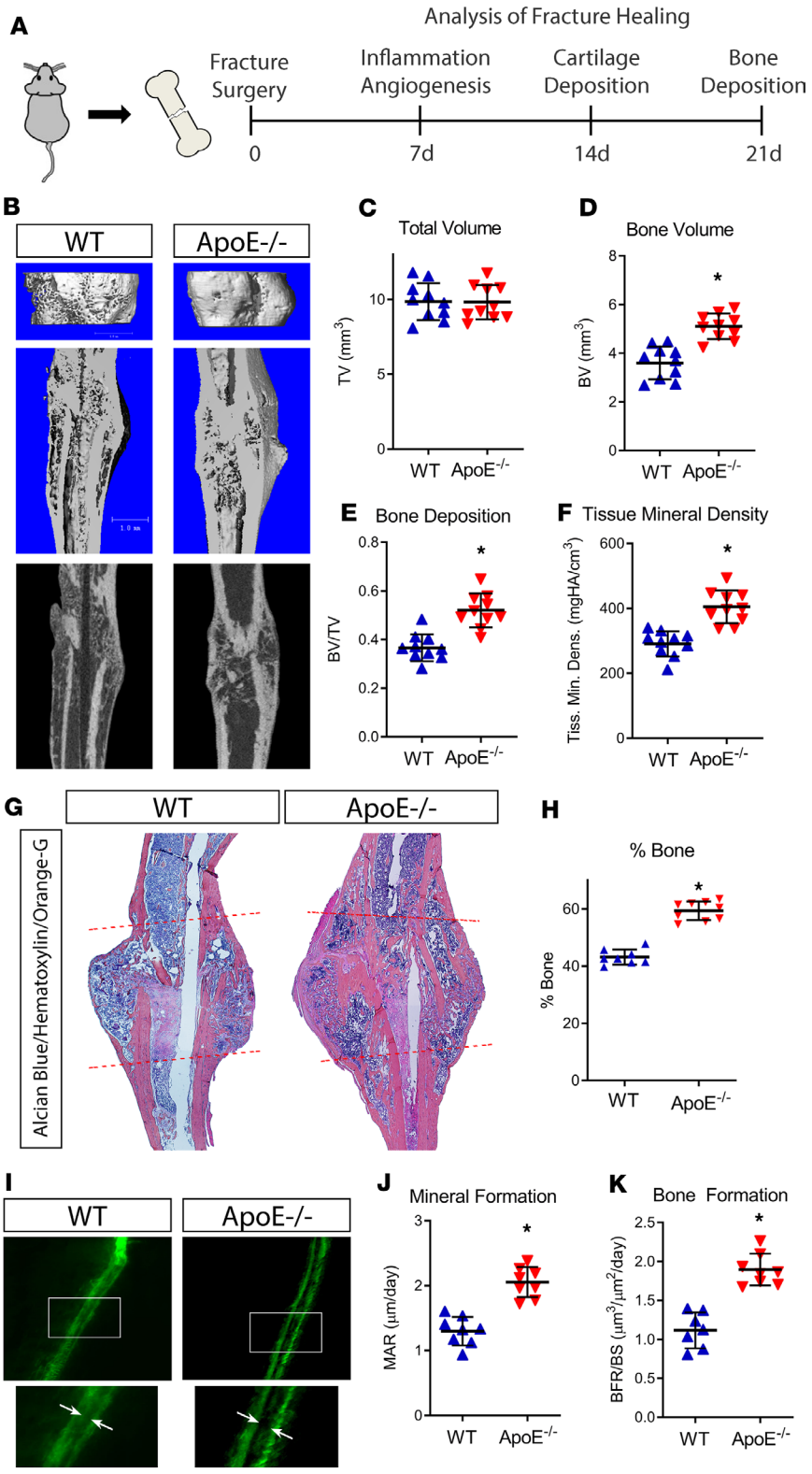

Figure 1. Loss of ApoE increases bone deposition during late stages of bone fracture healing. (**A**) Schematic diagram of tibial fracture model and subsequent assessment of repair. WT and ApoE$^{-/-}$ mice underwent tibial surgery, and fracture calluses were analyzed 7, 14, and 21 days after injury. (**B**) Using μCT, 21-day fracture calluses were assessed to determine (**C**) total callus volume (TV), (**D**) bone volume (BV), (**E**) bone content (BV/TV), and (**F**) tissue mineral density. Scale bar: 1 mm. (**G**) Histological staining with Alcian blue/hematoxylin/Orange G was used to visualize decalcified tissue (fracture callus region is indicated by dashed lines). (**H**) Histomorphometric analysis was used to quantify the amount of new bone within the fracture site and related to the total callus size. (**I**) Calcein double labeling (white arrows) was used to investigate the (**J**) mineral apposition rate (MAR) and (**K**) bone formation rate relative to the bone surface (BFR/BS). For μCT, histology, and histomorphometry, WT, n = 10; ApoE$^{-/-}$, n = 10. For calcein labeling, WT, n = 8; ApoE$^{-/-}$, n = 8. Data are expressed as mean ± 95% confidence interval. *P < 0.05, 2-tailed t test.

long bones of unfractured mice were adhered to tissue culture plastic. Upon adherence, cells were passaged and replated at equal density. Osteogenic media with and without recombinant apolipoprotein E (rApoE) were then used to differentiate these progenitor cells into osteoblasts (Figure 2A). Osteoblast differentiation was measured using ALP (a marker of osteoblastogenesis) stain, VK (a stain for mineralization) stain, and analysis of transcriptional osteogenic markers. ALP staining identified decreased osteoblast differentiation, and VK staining identified decreased mineralization in response to rApoE treatment (Figure 2B). Accordingly, evaluation of osteogenic transcripts from these differentiated cells via RT-PCR confirmed a 2-fold decrease in type I collagen (*Col1*), a 5-fold decrease in alkaline phosphatase (*Alp*), and a 4-fold decrease in bone sialoprotein (*Bsp*) in cells treated with rApoE (Figure 2C).

Importantly, differentiation of passaged bone marrow stromal cells from WT and ApoE$^{-/-}$ mice in osteogenic medium free of rApoE displayed no difference in ALP stain or VK stain (Supplemental Figure 4A). Within WT cultures, we investigated the expression of *ApoE* transcript using RT-PCR and compared this to *Col1* expression. *ApoE* transcript levels in WT cells did not change during differentiation (Supplemental Figure 4B). We also assessed ApoE protein within the culture systems using ELISA: ApoE protein was not detected in the growth media or within the cell lysates (Supplemental Figure 4C). Conversely, Schilling et al. observed ApoE expression during late stages (after 28 days) of in vitro osteogenic differentiation (14). This is likely a time at which differentiating osteoblasts have become encased in mineral and are more akin to osteocytes than to active osteoblasts. The

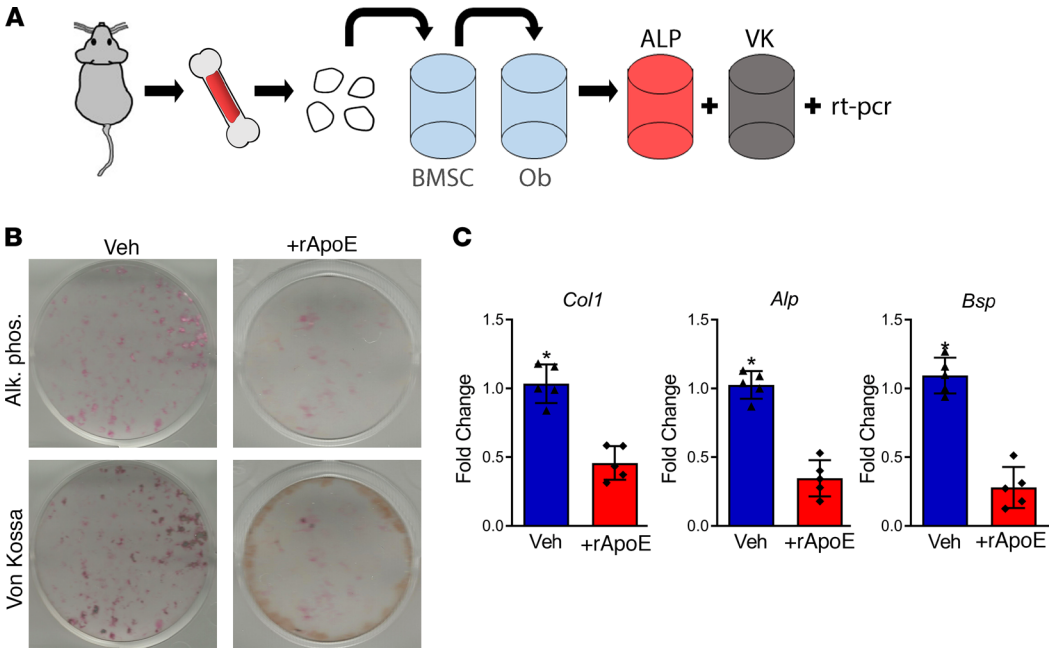

Figure 2. Treatment with rApoE decreases osteoblast differentiation. (**A**) Schematic diagram: bone marrow stromal cells (BMSCs) were aspirated from the long bones of WT mice and adhered to tissue culture plastic. After adhesion, cells were passaged to and differentiated to osteoblasts (Ob) by culturing in osteogenic medium for 14 days. ALP, alkaline phosphatase; VK, von Kossa. (**B**) Fixed, washed wells were assessed for alkaline phosphatase (Alk. Phos.) and for mineralization (Von Kossa). (**C**) Cell lysates were assessed for osteogenic transcripts (collagen I, *Col1*; alkaline phosphatase, *Alp*; and bone sialoprotein, *Bsp*) using RT-PCR. WT + vehicle, $n = 5$; WT + rApoE, $n = 5$. Data are expressed as mean ± 95% confidence interval. $^*P < 0.05$.

findings by Schilling et al. may be best explained by the fact that ApoE expression increases during cellular quiescence (21–23), a process that is likely occurring within osteoblasts during this late (28-day) time point. Collectively, these data indicate that osteoblasts are not a source of ApoE protein and that ApoE inhibits osteoblast differentiation and activity.

Treatment with rApoE decreases glycolytic metabolism during osteoblast differentiation. Work in the bone field has identified an important role for cellular metabolism with respect to osteoblast differentiation (24–29). Specifically, increased glycolytic metabolism is a prerequisite for robust osteoblast differentiation and mineralized matrix formation. Recently, ApoE has been reported to alter cellular metabolism in hematopoietic cells (30, 31). Here, we characterized the metabolic impact of rApoE on differentiating osteoblasts incubated with and without rApoE. Glycolytic metabolism of glucose to lactate was assessed by measurement of extracellular acidification rate (ECAR) (Figure 3A). Cultures treated with rApoE displayed dramatically lowered ECAR following glucose addition compared with vehicle-treated cells, demonstrating decreased basal glycolysis in cultures treated with rApoE (Figure 3B). We also observed that maximal glycolytic activity (glycolytic capacity), measured as the ECAR following addition of the F1/F0 ATPase inhibitor oligomycin (oligo), was also significantly decreased in rApoE-containing cultures compared with control cultures (Figure 3C). Finally, addition of 2-deoxyglucose (2DG), a potent glycolytic inhibitor, decreased the ECAR of both rApoE-treated and untreated osteoblast cultures to levels similar to those of preglucose ECAR, confirming that the changes in ECAR were due to glycolysis. Thus, our data clearly show that ApoE impairs glucose use in differentiating osteoblasts.

To better understand the mechanism underlying this decrease in glycolytic capacity, we determined whether there was a reduction in glucose uptake. Osteoblast cultures treated with and without rApoE were incubated with ^{3}H-2-deoxyglucose, and isotopically labeled glucose retained within the cells was quantified. Basal glucose uptake rates in rApoE-treated osteoblasts were 1.5-fold lower than in control cultures (Figure 3D). Next, we studied the expression of multiple key genes in the glycolytic pathway. Expression of multiple components of the glycolytic machinery was coordinately downregulated in osteoblasts treated with rApoE, including glucose transporter 1 (*Glut1*), hexokinase 2 (*Hk2*), aldolase A (*Aldoa*), enolase 3 (*Eno3*), lactate dehy-

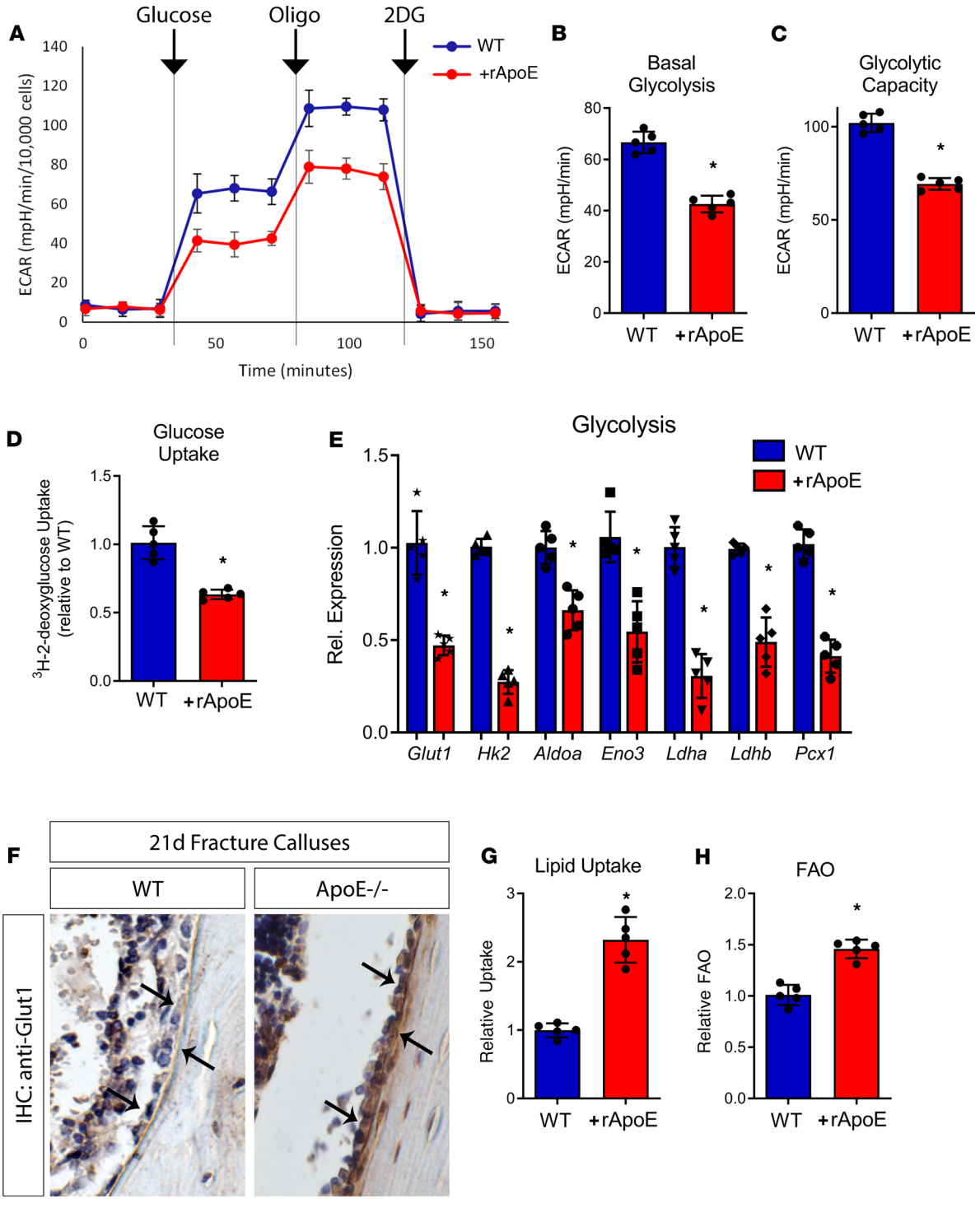

Figure 3. rApoE treatment decreases osteoblast glycolytic activity. WT osteoblasts differentiated in the absence and in the presence of rApoE were assessed for metabolic changes. (**A**) The Seahorse XF24 extracellular flux metabolic analyzer was used to measure the extracellular acidification rate (ECAR) in response to the addition of glucose, oligomycin (oligo), and 2-deoxyglucose (2DG). These observations were used to determine (**B**) basal glycolysis and (**C**) glycolytic capacity. (**D**) Glucose uptake was measured by pulsing differentiating osteoblasts with ^{3}H-2-deoxyglucose. (**E**) Transcript levels of key genes involved in glycolytic metabolism were assessed using RT-PCR. (**F**) Immunohistochemistry was used to investigate the level of Glut1 in healing, 21-day fracture calluses (osteoblasts indicated by arrows). (**G**) Lipid uptake in cultures was measured in both the absence and presence of rApoE as was (**H**) fatty acid oxidation (FAO). For metabolic flux experiments, WT + vehicle, $n = 5$; WT + rApoE, $n = 5$. For RT-PCR, WT + vehicle, $n = 6$; WT + rApoE, $n = 6$. For IHC, WT, $n = 4$; ApoE$^{-/-}$, $n = 4$. For lipid uptake and FAO, WT + vehicle, $n = 6$, WT + rApoE, $n = 6$. Data are expressed as mean ± 95% confidence interval. *$P < 0.05$.

drogenase A (*Ldha*), lactate dehydrogenase B (*Ldhb*), and pyruvate carboxylase 1 (*Pcx1*) (Figure 3E). Thus, the decrease in glycolytic capability in response to rApoE treatment likely results from decreased expression of key glycolytic enzymes and lower rates of glucose uptake. These in vitro findings were further substantiated in vivo by immunohistochemistry data showing higher staining for Glut1 in osteoblasts lining the bone in fracture calluses from ApoE$^{-/-}$ mice (Figure 3F).

Because ApoE in circulation is known to take part in the formation of chylomicrons to transport lipids in the body, we hypothesized that increased circulating ApoE levels might enhance lipid uptake and fatty acid oxidation within osteoblasts to offset decreased glycolytic metabolism. To test this hypothesis, we investigated lipid uptake in differentiating osteoblast cultures differentiated with and without rApoE. Indeed, we found that relative to untreated controls, rApoE treatment more than doubled the amount of lipid uptake (Figure 3G) and increased fatty acid oxidation (FAO, Figure 3H).

These data confirm a regulatory role for ApoE in osteoblast metabolism. They indicate that the enhanced bone healing observed in the absence of ApoE is due to increased glycolytic metabolism and subsequent enhanced differentiation of osteoblasts. Conversely, in the presence of ApoE, osteoblasts increase fatty acid catabolism and decrease glycolytic metabolism, leading to decreased osteoblast differentiation.

Circulating ApoE hinders robust fracture healing. Our data indicate that ApoE plays an inhibitory role during fracture healing and osteoblast differentiation, but ApoE is not expressed by osteoblasts themselves. In the body, the majority of ApoE is found within the circulation (32). To determine whether circulating ApoE affects fracture healing, we used our parabiosis models, anastomosing WT mice to either WT mice or ApoE$^{-/-}$ mice, and investigated fracture healing in WT mice (Figure 4A). Circulating ApoE levels were measured using ELISA on serum from each mouse within the pairings isolated at 21 days after injury. Bone repair was assessed using μCT and histological analysis on 21-day fracture calluses from the WT mice. Serum of WT mice anastomosed to ApoE$^{-/-}$ mice contained half the level of ApoE relative to the serum of WT mice anastomosed to WT mice (Figure 4B). Importantly, fracture healing of WT mice anastomosed to ApoE$^{-/-}$ mice was improved (Figure 4C). μCT analysis demonstrated both BV/TV and tissue mineral density of WT mice anastomosed to ApoE$^{-/-}$ mice to be higher than those of WT mice anastomosed to WT mice (Figure 4, D and E). Histomorphometry of decalcified, paraffin-embedded sections stained with Alcian blue/hematoxylin/Orange G supported these findings (Figure 4F). μCT values for BV/TV and tissue mineral density for this WT-ApoE$^{-/-}$ group were similar to the μCT values observed for solitary ApoE$^{-/-}$ mice in Figure 1.

Importantly, combining the circulation of ApoE$^{-/-}$ mice with the circulation of WT mice increased circulating ApoE levels within ApoE$^{-/-}$ animals (Supplemental Figure 5A) but did not translate to a measurable change in fracture healing (Supplemental Figure 5B). We propose that this finding identifies that ApoE levels exist within a critical threshold, which when surpassed, diminishes bone fracture healing. Collectively, these data indicate that circulating ApoE plays a strong inhibitory role during fracture healing.

Circulating ApoE increases with age. Because of the impaired fracture healing seen with age and our previous observation that ApoE may be differentially expressed in aged cell culture systems, we investigated the effect of age on circulating ApoE levels. We used ELISA to measure the amount of ApoE in the serum of young patients (35–45 years old) and old patients (75–85 years old) and the serum of young mice (4 months old) and aged mice (24 months old). In patients, ApoE levels were 2-fold higher in the geriatric population than in the young population (Figure 5A). Similarly, circulating ApoE levels in aged mice were 3-fold higher than in young mice (Figure 5B). These findings demonstrate that circulating ApoE levels increase with age.

Decreasing ApoE in circulation improves aged fracture healing. Based on our findings that circulating ApoE levels increase with age (Figure 5) and that circulating ApoE inhibits bone healing (Figure 4), we hypothesized that the age-related increase in circulating ApoE results in impairment in bone fracture healing. To test this hypothesis, we investigated whether decreasing circulating ApoE levels in aged mice would improve aged bone fracture healing. Approximately 90% of ApoE in the body is generated by hepatocytes and secreted into circulation (32); therefore, to lower circulating ApoE levels, we used an siRNA system driven by adeno-associated virus(serotype 8) (AAV[serotype8]), a serotype that shows specificity for the liver (33, 34). AAV(serotype 8)-GFP-siRNA-ApoE (siRNA-ApoE) or AAV(serotype 8)-GFP (GFP) were injected into the tail vein of 24-month-old mice 3 days before fracture surgery (Figure 6A); fracture calluses and serum were harvested 21 days after injury. By ELISA, serum levels of ApoE in mice treated with siRNA-ApoE were approximately 75% lower than in mice treated with the GFP control (Figure 6B). μCT analysis demonstrated that fracture calluses from siRNA-ApoE–treated mice had higher levels of BV/TV and a higher tissue mineral density than those of GFP control (Figure 6, C–E). To test whether this increase

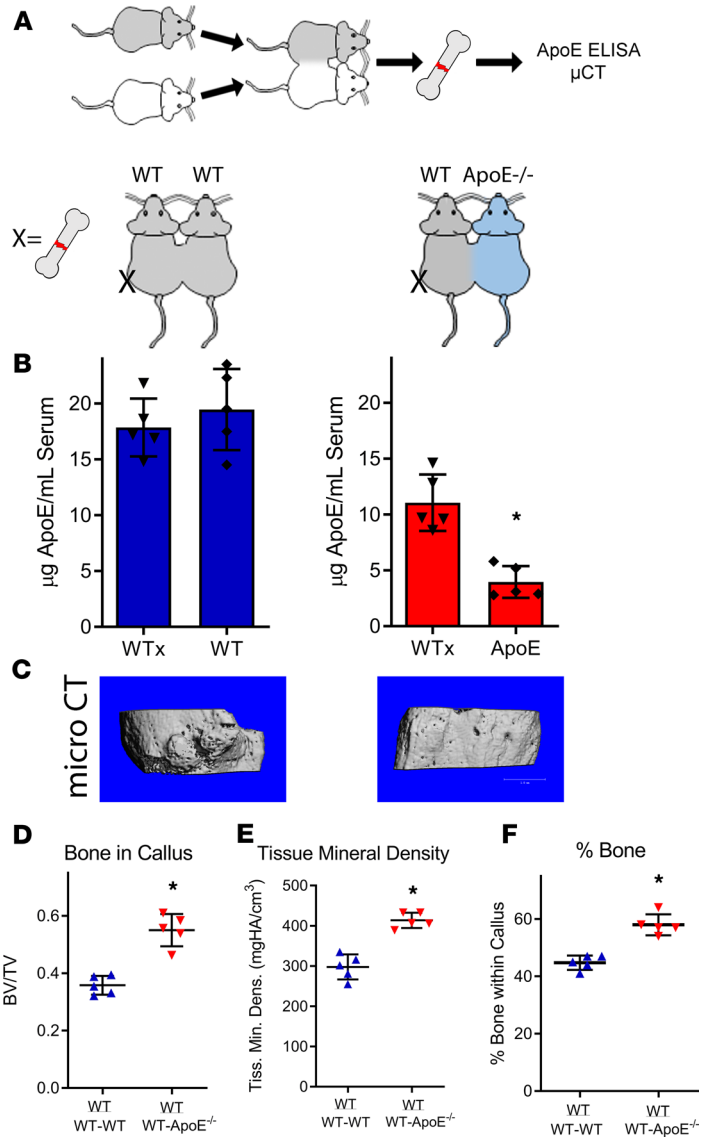

Figure 4. Circulating ApoE inhibits bone fracture healing. (**A**) Schematic diagram: WT and ApoE$^{-/-}$ mice were anastomosed together, resulting in a shared blood supply. (**B**) After 4 weeks of anastomosis, ELISA was used to measure circulating ApoE levels within each mouse. (**C**) One WT mouse within each pairing underwent tibial fracture surgery, and fracture calluses were assessed 21 days after injury for healing. Scale bar: 1 mm. (**D**) Bone ratio within the callus and (**E**) tissue mineral density of the callus were measured using μCT and (**F**) histomorphometry (decalcified, paraffin embedded, Alcian blue/hematoxylin/Orange G stain) was used to quantify the amount of bone tissue deposited within the fracture callus. For both WT-WT pairs and for WT-ApoE$^{-/-}$ pairs, n = 5. Data are expressed as mean ± 95% confidence interval. *$P < 0.05$.

in bone deposition translates to improved fracture healing, mechanical testing was conducted on tibiae 28 days after fracture. Healed tibiae from aged mice treated with siRNA-ApoE displayed higher levels of maximal force to refracture and increased structural stiffness (Figure 6, F and G).

Aged fracture healing is associated with increased fibrotic tissue deposition. In our previous work, rejuvenation of aged fracture healing involved decreased fibrotic tissue deposition within the fracture callus coupled with increased bone deposition (35). We identified regions of fibrous deposition within our ApoE-knockdown experiment by staining decalcified, paraffin-embedded histological sections with Alcian blue/hematoxylin/Orange G. Although fibrosis was identified within the fracture callus of control/GFP–treated mice (arrows, Figure 6H), areas of fibrosis were absent in aged mice treated with siRNA-ApoE, and, in contrast, these calluses contained newly deposited bone tissue (arrows, Figure 6I). Indeed, histomorphometry demonstrated the siRNA-ApoE group to have increased bone deposition within the fracture callus compared with the control/GFP group (Figure 6J). Importantly, as a control, aged ApoE$^{-/-}$ mice did not display a fracture callus phenotype in response to siRNA-ApoE treatment (Supplemental Figure 6, A–C).

Collectively, these data demonstrate that with age, there is an increase in the circulating ApoE levels, leading to decreased osteoblast differentiation and impaired bone fracture healing (Supplemental Figure 6D). Moreover, upon lowering these ApoE levels, bone fracture healing is substantially improved.

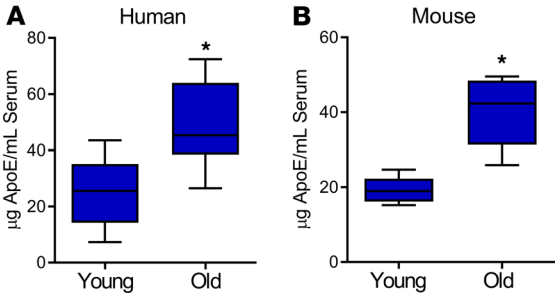

Figure 5. Circulating ApoE levels in humans and in mice increase with age. Serum collected from (**A**) humans (young, 35–45 years of age; old 75–85 years of age) and from (**B**) mice (young, 4 months old; old, 24 months old) was assessed for total ApoE protein using ELISA. Young patients, $n = 17$; old patients, $n = 34$; young mice, $n = 7$; old mice, $n = 7$. Data are expressed as mean ± 95% confidence interval. $^*P < 0.05$.

Discussion

It has long been observed that bone fracture healing diminishes with age. The growing geriatric population and the comorbidities associated with injury during advanced age have inspired a resurgence in the number of studies investigating age-related changes in tissue regeneration (36–39). Indeed, our previous work identified a key role for circulation in the age-associated decrease in bone regeneration (35). Although much of the attention stemming from this work has focused on "youth factors," follow-up investigations analyzing "aging factors" have been lacking.

Here we identify ApoE as an aging factor. We found that ApoE levels in circulation increase with age in humans and in mice and directly impair fracture healing and bone regeneration. In vivo, circulating ApoE inhibited bone deposition within the injury site, and in vitro, exogenous treatment with rApoE inhibited osteoblast differentiation. By using targeted strategies, we were able to lower circulating ApoE levels in aged mouse models, which subsequently led to improved bone regeneration. Mice in which circulating ApoE was decreased displayed increased bone deposition and decreased fibrotic tissue within the healing fracture callus and increased mechanical strength.

We have identified changes in circulating ApoE levels that affect osteoblast biology and subsequently bone fracture healing. Although others have observed a potential role for ApoE in inflammation (40, 41), angiogenesis (42, 43), and even cartilage formation within the vasculature during atherosclerosis (44, 45), we observed none of these changes in our model of bone fracture healing. We postulate that this apparent discrepancy may be due to the fact that although others have observed ApoE's influence during homeostatic conditions, bone fracture injury represents an acute and severe event that triggers a unique biological response. For this reason, it has historically been difficult to identify modulators of tissue regeneration using homeostatic systems. Here, the major effect that we observed in multiple mouse models of fracture healing were changes in bone deposition. In vivo we observed ApoE to inhibit bone formation and mineral apposition, and in vitro we observed rApoE to decrease osteoblast differentiation and mineral formation.

Differentiating osteoblasts actively engaged in bone formation have previously been shown to rely primarily on glycolysis for energy accrual (26, 27). Here we demonstrate that ApoE promotes concomitant reductions in glycolytic metabolism while promoting FAO, which leads to subsequent inhibition of fracture healing and a decrease in osteoblast differentiation and activity.

Our findings serve as a proof of concept for potential translation to therapies in which circulating ApoE is decreased after injury or after surgery to improve bone healing; we envision an acute intervention, given that chronic lowering of ApoE levels may have negative effects. Indeed, chronic loss of ApoE in mouse models has been shown to be detrimental to cardiovascular health (6, 46) and neuronal biology (47, 48). Nevertheless, the work presented here highlights ApoE as a potentially novel therapeutic target to be explored in strategies aimed at enhancing bone healing. Our findings suggest that temporally lowering ApoE levels may represent a novel therapeutic approach to enhance bone formation to improve bone healing and the osseous integration of implants following fracture or surgical procedures.

Methods

Mouse models. All protocols were approved by the Duke Institutional and Animal Care and Use Committee. $ApoE^{-/-}$ mice (B6.129P2-Apoetm1Unc/J, stock 2052) were purchased from Jackson Laboratories and crossed with $ApoE^{+/+}$ mice (C57BL/6J, stock 000664) to generate $ApoE^{+/-}$ breeders. Mice were then crossed using a breeding strategy of heterozygous × heterozygous. Genotype was ensured using DNA PCR

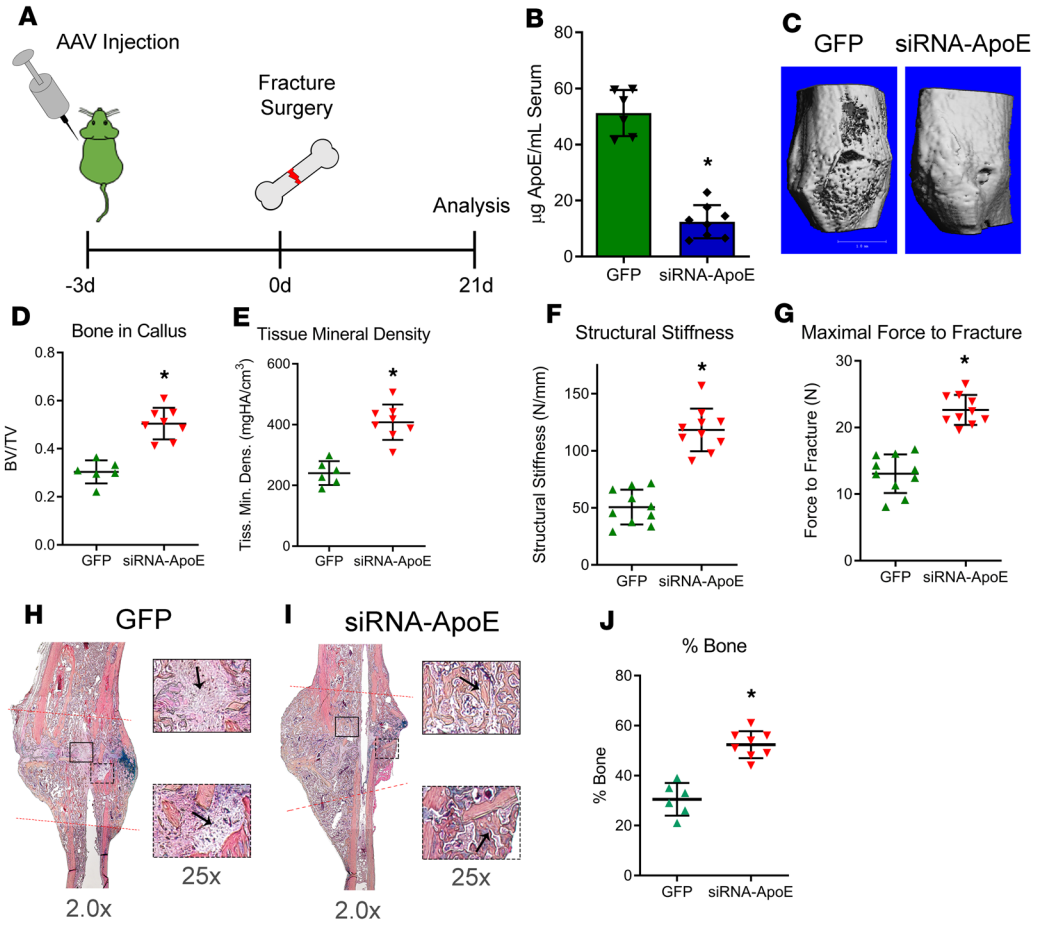

Figure 6. Decreasing circulating ApoE levels improves bone regeneration in aged mouse models. (**A**) Schematic diagram: 24-month-old mice were injected with AAV carrying either GFP or siRNA-ApoE. Mice underwent tibial fracture surgery and were allowed to heal for 21 days. (**B**) Using ELISA, 24 days after injection, circulating ApoE levels were measured within the serum of mice. (**C**) Using µCT, 21-day fracture calluses were assessed for (**D**) bone ratio within the callus and (**E**) tissue mineral density. Scale bar: 1 mm. Mechanical testing was performed on 28-day fracture calluses to assess (**F**) structural stiffness and (**G**) maximal force to fracture. (**H** and **I**) Alcian blue/hematoxylin/Orange G staining was performed on decalcified, paraffin-embedded sections. Areas of fibrous tissue (**H**, GFP, arrows) and areas of bone deposition (**I**, siRNA-ApoE, arrows) are depicted at indicated original magnifications. (**J**) Histomorphometry was used to measure the amount of bone tissue deposited within the healing fracture callus. For GFP, $n = 6$; for siRNA-ApoE, $n = 8$. Data are expressed as mean ± 95% confidence interval. $^*P < 0.05$.

from ear punch tissue or tail fragment using a combination of common primer (5′-GCCTAGCCGAGGGAGAGCCG-3′), wild-type primer (5′-TGTGACTTGGGAGCTCTGCAGC-3′), or mutant primer (5′-GCCGCCCCGACTGCATCT-3′). WT (ApoE$^{+/+}$) mice and ApoE$^{-/-}$ mice were used for fracture analysis studies and osteoblast differentiation studies.

Tibial fracture surgery. Fractures were performed as previously described (18, 19). Briefly, 4-month-old or 24-month-old mice were anesthetized, and the surgical area proximal to the knee was shaved and disinfected. Following an incision, a hole was drilled into the tibial plateau, and a 0.7-mm stainless steel pin was placed into the medullary cavity and cut flush with the tibial plateau. A tibial fracture was induced midshaft using blunt scissors, and the incision was closed using wound clips. For analgesia, 0.5 mg/kg buprenorphine–sustained release was administered subcutaneously at the beginning of the procedure.

Parabiosis surgery. Anastomosis was achieved as previously described (18). Briefly, WT or ApoE$^{-/-}$ littermate mice were weaned into the same cage as separate pairs. At 3 months of age, the mice underwent parabiosis surgery and were allowed to heal for 4 weeks, at which time the mice underwent tibial fracture surgery. Fracture calluses were isolated 21 days after injury and investigated using µCT and histological analysis. Note, only female mice were used within parabiosis models.

siRNA-ApoE (AAV) treatment of aged mice. AAV(serotype 8) carrying a vector expressing either sh-RNA-ApoE or GFP (Vectoc Biosystems Inc.) was injected into the tail vein of a 24-month-old mouse at 1×10^{13}

GC/mouse. After 4 days, mice underwent tibial fracture surgery, and fracture calluses were harvested 21 days after injury. At the time of callus harvest, blood was also collected to assay for ApoE protein within the serum using ELISA.

Immunoassays. Inflammatory biomarkers, angiogenic biomarkers, and ApoE protein content were quantified by ELISA. Custom multiplex assays were performed to measure mouse proinflammatory markers (IL-1β, IL-6, KC, IL-10, TNF-α) and cytokines (MCP-1, MIP-1α) (MesoScale Discovery) in serum samples (diluted 2- and 4-fold, respectively). Mean reported intra- and interassay coefficients of variation for these assays were all less than 10% and less than 12%, respectively. Angiogenic markers (VCAM, VEGF) (R&D Systems Inc.) were measured in serum samples and fracture callus tissue lysates (diluted 50-fold and 20-fold for measurement of VCAM, respectively, and diluted 5-fold for measurement of VEGF). ApoE levels were measured from serum of mice (Abcam, ab215086) and patients (Invitrogen Inc., EHAPOE) as per manufacturers' instructions. Mean reported intra- and interassay coefficients of variation for these assays were all less than 10% and less than 12%, respectively.

Analysis of fracture healing. Fracture calluses were dissected and fixed in 10% Zn-formalin at room temperature for 5 days. μCT analysis was conducted using a Scanco vivaCT 80 (Scanco Medical) at a scan resolution of 8 μm. Fractured tibiae were scanned and the midpoint of the fracture callus was identified by meticulously assessing the radiographic slices within the fracture callus — this could be determined by scanning through the slices of the callus and visually identifying the proximal and distal boarders of intact cortical bone within the fracture callus. These boundaries represent the entire fracture region. The midpoint of this fracture region was defined as the fracture site. Calluses were analyzed 1 mm proximal and 1 mm distal from the fracture site and assessed for TV and BV in mm^3, percentage of BV per TV, and bone mineral density in mg HA/mm^3. Fixed fracture calluses were decalcified using 12% EDTA at pH 7.4, cleared of EDTA, and embedded into paraffin. Sections were cut at a thickness of 5 μm and stained using Alcian blue/hematoxylin/Orange G (MilliporeSigma) to visualize bone and cartilage. A minimum of 5 sections were used to conduct computer-assisted histomorphometry analysis, and results were presented as an amount relative to the total area of the fracture callus. TRAP staining was performed as previously described (49). TRAP-positive cells were quantified as the percentage of osteoclast surface to bone surface. Fluorochrome labeling was used to investigate active bone deposition. Calcein green (30 mg/kg/g) (MilliporeSigma) in saline was delivered using peritoneal injections at 4 days and 1 day before harvest of the fracture callus. Specimens were fixed in 70% ethanol and embedded in methyl methacrylate. Sections were then cut to 5 mm, and fluorescent microscopy imaging (495 nm/521 nm, fluorescein isothiocyanate) was used to observe the dye; the distance between the dye fronts was measured using an Olympus IX70 microscope and associated Olympus cellScens Standard 1.16 software (Olympus Corporation). Glut1 immunohistochemistry was performed using Glut1 antibody (Abcam, ab15309) as per the manufacturer's instructions.

Mechanical testing. The healing tibiae of mice were harvested 28 days after fracture surgery and wrapped in PBS-soaked gauze and stored at –80°C. In preparation for mechanical testing, tibiae were allowed to come to room temperature by placing them into fresh room temperature PBS for 2 hours. Samples were tested in 4-point bending in the medial-lateral direction with the medial side in tension using an ElectroForce 3220 Series III instrument (TA Instruments). Cylindrical rollers 2 mm in diameter were used to apply the 4 points of loading. The midpoints of the top 2 rollers were positioned 4 mm apart while the midpoints of the bottom 2 rollers were positioned 10 mm apart. The top fixture was able to tilt horizontally to allow for simultaneous contact between all 4 rollers and the sample. To position each tibia within the 4-point bending fixture, the most proximal location of the tibia-fibula junction was aligned with the outer edge of 1 of the bottom loading rollers, ensuring the fracture callus was centered among all rollers. Bending failure tests were performed in displacement control at a rate of 0.025 mm/s. Testing was terminated by failure, as determined by a 95% drop in load.

Load, displacement, and time were recorded at a sampling frequency of 10 Hz. Structural stiffness (N/mm) was calculated as the slope of the load versus displacement data between 30% and 70% of the load at failure, to exclude nonlinear toe regions in the force displacement curves. Force to fracture was identified as the load maximal which occurred before failure.

Bone marrow stromal cell culture. Unfractured mice were euthanized at 4 months of age, and the femurs and tibiae were dissected and cleaned of soft tissue. Bone marrow was flushed from the long bones, and cells were plated at a density of $500 \times 10^3/cm^2$ in plating medium (AMEM, 10% FBS, 100 U/mL penicillin/streptomycin) for 7 days. Cells were then differentiated to osteoblasts in osteogenic medium (AMEM,

10% FBS, 100 U/mL penicillin/streptomycin, 30 μM ascorbic acid, 10^{-8} M dexamethasone, 8 mM sodium phosphate) with or without rApoE (100 ng/mL). After 15 days in differentiation medium, wells were washed with PBS, fixed using 10% formalin, and stained for ALP using FastRed (MilliporeSigma) or for mineral using 2.5% silver nitrate solution (VK) on a light box. Replicate wells were washed with PBS, and RNA was extracted using TRIzole Reagent (Invitrogen Inc.) as per manufacturer's protocol.

Real-time PCR. After RNA extraction, purity and quantity of RNA were determined using spectrometric methods. cDNA template was generated using random hexamers. TaqMan primers for *Alp* (Mm00475834_m1), *BSP* (Mm00492555_m1), *Col1* (Mm00801666_g1), *Aldoa* (Mm00833172_g1), *Hk2* (Mm00443385_m1), *Ldha* (Mm01612132_g1), *Ldhb* (Mm01267402_m1), and *Eno3* (Mm00468267_m1) were purchased from Applied Biosystems, and samples were investigated using a ViiA 7 Real-Time PCR System and compared to the transcript of ribosomal protein 18S as a housekeeping control. A minimum of 5 replicates of all samples were analyzed.

Metabolic flux analysis. ECAR and oxygen consumption rate of osteoblastic cultures were determined using the Seahorse XF24 assay system (Agilent Technologies). Bone marrow stromal cells were plated as stated above, and after adherence, the cells were lifted using trypsin digestion and passaged to a concentration of 160,000 cells per well. This ensured similar number of plated cells in both WT ($ApoE^{+/+}$) and $ApoE^{-/-}$ cultures. Cells were cultured in osteogenic medium for 7 days. Before metabolic analysis, medium was replaced with XF Assay Media supplemented with 1% FBS. In flux analysis that investigated glycolytic metabolism, glucose, oligo, and 2DG were injected for a final concentration of 10 mM, 1.0 μM, and 50 mM, respectively, at the indicated times (32 minutes, 74 minutes, and 117 minutes). In flux analysis that investigated oxidative phosphorylation, base media containing 5.5 mM glucose and oligo, FCCP, and antimycin were injected for a final concentration of 1.0 μM, 1.0 μM, and 0.5 μM, respectively, at the indicated times (32 minutes, 74 minutes, and 117 minutes).

Glucose uptake assay. Glucose uptake was determined by pulsing 0.5 mCi/mL ^{3}H-2-deoxyglucose and 100 mM 2DG in cell cultures after 1 hour of glucose-free fasting. After 90 minutes of incubation, wells were washed 5 times with PBS, and contents were extracted in protein lysis buffer. The amount of ^{3}H-2-deoxyglucose was quantified using a liquid scintillation counter and related to WT control.

Lipid uptake and FAO assay. Bone marrow aspirates were cultured and passaged as described above. Cells were passaged into a black, clear-bottom tissue culture plate (Invitrogen Inc.) at 5×10^4 cells per well. Bone marrow stromal cells were differentiated in osteogenic media. After 7 days in differentiation media, media were changed to contain either no rApoE or 100 nM rApoE for 2 days. Fatty acid uptake was then assessed over a 120-minute period using a Fatty Acid Uptake Kit (MilliporeSigma, MAK156). Lipid uptake was then measured using fluorescent measurement (excitation wavelength [λ_{ex}] = 485 nm, emission wavelength [λ_{em}] = 515 nm). Results were represented as relative quantities. FAO was measured using a Fatty Acid Oxidation Assay kit (Abcam, ab217602). Wells were washed twice with fatty acid free assay media and incubated overnight with or without rApoE in fatty acid measurement media containing oxygen consumption reagent. Oxygen consumption in response to FAO was then measured (λ_{ex} = 380 nm, λ_{em} = 650 nm). Results were represented as relative quantities.

Patient samples. Serum samples were obtained with informed consent from a cohort of patients used in Kraus et al. (50). Blood was collected from participants by venipuncture 2 hours postprandial and separated by centrifugation at 1500 *g* for 15 minutes to yield serum and plasma samples that were stored as aliquots at –80°C until analyzed. To best model our mouse data at 4 months and 24 months of age, patients aged 35–45 years were declared the "young" group while patients aged 75–85 were declared the "aged" group (51).

Statistics. All statistical analysis was performed using GraphPad PRISM 5 (version 5.01). Data are expressed as mean ± 95% confidence interval. Groups were compared using independent 2-tailed *t* tests. Statistical significance was assigned to *P* values less than 0.05.

Study approval. For patient samples, all procedures were approved by the Duke University Institutional Review Board with informed consent being obtained from all subjects. For mouse models, all procedures were approved by the Duke Institutional and Animal Care and Use Committee.

Author contributions

RH, XZ, PN, JLH, JPW, and GSB performed experiments. RH, XZ, JLH, JPW, and GSB performed data analysis. GSB performed surgeries. PJW and GSB designed the study. VBK, PJW, and GSB drafted the manuscript.

Acknowledgments

The authors would like to thank Natalie Pang for help with manuscript preparation and editing and Christopher Newgard for manuscript suggestions and Tim Koves for his excellent technical assistance with the Seahorse Metabolic Flux Assay system. JPW and VBK are funded by Duke Aging Center/Pepper Center grants AG028716 and K01AG056664. PJW is funded by a Pathway to Stop Diabetes Initiator Award from the American Diabetes Association (1-16-INI-17). This work was funded in part by a Borden Scholar Award to GSB.

Address correspondence to: Gurpreet S. Baht, Duke Molecular Physiology Institute, 300 North Duke Street, Durham, North Carolina 27701, USA. Phone: 919.681.2864; Email: gurpreet.baht@duke.edu.

1. Burge R, Dawson-Hughes B, Solomon DH, Wong JB, King A, Tosteson A. Incidence and economic burden of osteoporosis-related fractures in the United States, 2005–2025. *J Bone Miner Res*. 2007;22(3):465–475.
2. Baht GS, Vi L, Alman BA. The role of the immune cells in fracture healing. *Curr Osteoporos Rep*. 2018;16(2):138–145.
3. Giannoudis PV, Jones E, Einhorn TA. Fracture healing and bone repair. *Injury*. 2011;42(6):549–550.
4. Vi L, et al. Macrophage cells secrete factors including LRP1 that orchestrate the rejuvenation of bone repair in mice. *Nat Commun*. 2018;9(1):5191.
5. Mahley RW. Apolipoprotein E: cholesterol transport protein with expanding role in cell biology. *Science*. 1988;240(4852):622–630.
6. Nakashima Y, Plump AS, Raines EW, Breslow JL, Ross R. ApoE-deficient mice develop lesions of all phases of atherosclerosis throughout the arterial tree. *Arterioscler Thromb*. 1994;14(1):133–140.
7. Plump AS, et al. Severe hypercholesterolemia and atherosclerosis in apolipoprotein E-deficient mice created by homologous recombination in ES cells. *Cell*. 1992;71(2):343–353.
8. Davignon J, Gregg RE, Sing CF. Apolipoprotein E polymorphism and atherosclerosis. *Arteriosclerosis*. 1988;8(1):1–21.
9. Zhang SH, Reddick RL, Piedrahita JA, Maeda N. Spontaneous hypercholesterolemia and arterial lesions in mice lacking apolipoprotein E. *Science*. 1992;258(5081):468–471.
10. Coon KD, et al. A high-density whole-genome association study reveals that APOE is the major susceptibility gene for sporadic late-onset Alzheimer's disease. *J Clin Psychiatry*. 2007;68(4):613–618.
11. Namba Y, Tomonaga M, Kawasaki H, Otomo E, Ikeda K. Apolipoprotein E immunoreactivity in cerebral amyloid deposits and neurofibrillary tangles in Alzheimer's disease and kuru plaque amyloid in Creutzfeldt-Jakob disease. *Brain Res*. 1991;541(1):163–166.
12. Corder EH, et al. Gene dose of apolipoprotein E type 4 allele and the risk of Alzheimer's disease in late onset families. *Science*. 1993;261(5123):921–923.
13. Cauley JA, et al. Apolipoprotein E polymorphism: a new genetic marker of hip fracture risk — The Study of Osteoporotic Fractures. *J Bone Miner Res*. 1999;14(7):1175–1181.
14. Schilling AF, et al. Increased bone formation in mice lacking apolipoprotein E. *J Bone Miner Res*. 2005;20(2):274–282.
15. Shiraki M, et al. Association of bone mineral density with apolipoprotein E phenotype. *J Bone Miner Res*. 1997;12(9):1438–1445.
16. Zhang SQ, Zhang WY, Ye WQ, Zhang LJ, Fan F. Apolipoprotein E gene E2/E2 genotype is a genetic risk factor for vertebral fractures in humans: a large-scale study. *Int Orthop*. 2014;38(8):1665–1669.
17. Bartelt A, et al. Apolipoprotein E-dependent inverse regulation of vertebral bone and adipose tissue mass in C57Bl/6 mice: modulation by diet-induced obesity. *Bone*. 2010;47(4):736–745.
18. Xiong C, Zhang Z, Baht GS, Terrando N. A mouse model of orthopedic surgery to study postoperative cognitive dysfunction and tissue regeneration. *J Vis Exp*. 2018;(132):56701.
19. Baht GS, Nadesan P, Silkstone D, Alman BA. Pharmacologically targeting beta-catenin for NF1 associated deficiencies in fracture repair. *Bone*. 2017;98:31–36.
20. Wei X, Zhang Y, Zhou J. Alzheimer's disease-related gene expression in the brain of senescence accelerated mouse. *Neurosci Lett*. 1999;268(3):139–142.
21. Ang LS, Cruz RP, Hendel A, Granville DJ. Apolipoprotein E, an important player in longevity and age-related diseases. *Exp Gerontol*. 2008;43(7):615–622.
22. Quinn CM, et al. Induction of fibroblast apolipoprotein E expression during apoptosis, starvation-induced growth arrest and mitosis. *Biochem J*. 2004;378(pt 3):753–761.
23. Fukada S, et al. Molecular signature of quiescent satellite cells in adult skeletal muscle. *Stem Cells*. 2007;25(10):2448–2459.
24. Frey JL, Kim SP, Li Z, Wolfgang MJ, Riddle RC. β-Catenin directs long-chain fatty acid catabolism in the osteoblasts of male mice. *Endocrinology*. 2018;159(1):272–284.
25. Frey JL, et al. Wnt-Lrp5 signaling regulates fatty acid metabolism in the osteoblast. *Mol Cell Biol*. 2015;35(11):1979–1991.
26. Wei J, et al. Glucose uptake and Runx2 synergize to orchestrate osteoblast differentiation and bone formation. *Cell*. 2015;161(7):1576–1591.
27. Guntur AR, et al. Osteoblast-like MC3T3-E1 cells prefer glycolysis for ATP production but adipocyte-like 3T3-L1 cells prefer oxidative phosphorylation. *J Bone Miner Res*. 2018;33(6):1052–1065.
28. Lee WC, Guntur AR, Long F, Rosen CJ. Energy metabolism of the osteoblast: implications for osteoporosis. *Endocr Rev*. 2017;38(3):255–266.
29. Li Z, et al. Glucose transporter-4 facilitates insulin-stimulated glucose uptake in osteoblasts. *Endocrinology*. 2016;157(11):4094–4103.
30. Sun W, et al. Macrophage inflammasome mediates hyperhomocysteinemia-aggravated abdominal aortic aneurysm. *J Mol Cell Cardiol*. 2015;81:96–106.
31. Sarrazy V, et al. Disruption of Glut1 in hematopoietic stem cells prevents myelopoiesis and enhanced glucose flux in atheroma-

tous plaques of ApoE(–/–) mice. *Circ Res*. 2016;118(7):1062–1077.
32. Kraft HG, Menzel HJ, Hoppichler F, Vogel W, Utermann G. Changes of genetic apolipoprotein phenotypes caused by liver transplantation. Implications for apolipoprotein synthesis. *J Clin Invest*. 1989;83(1):137–142.
33. Davidoff AM, et al. Comparison of the ability of adeno-associated viral vectors pseudotyped with serotype 2, 5, and 8 capsid proteins to mediate efficient transduction of the liver in murine and nonhuman primate models. *Mol Ther*. 2005;11(6):875–888.
34. Fang CC, Wu CF, Liao YJ, Huang SF, Chen M, Chen YA. AAV serotype 8-mediated liver specific GNMT expression delays progression of hepatocellular carcinoma and prevents carbon tetrachloride-induced liver damage. *Sci Rep*. 2018;8(1):13802.
35. Baht GS, et al. Exposure to a youthful circulaton rejuvenates bone repair through modulation of β-catenin. *Nat Commun*. 2015;6:7131.
36. Almada AE, Wagers AJ. Molecular circuitry of stem cell fate in skeletal muscle regeneration, ageing and disease. *Nat Rev Mol Cell Biol*. 2016;17(5):267–279.
37. Brack AS. Ageing of the heart reversed by youthful systemic factors! *EMBO J*. 2013;32(16):2189–2190.
38. Brack AS, et al. Increased Wnt signaling during aging alters muscle stem cell fate and increases fibrosis. *Science*. 2007;317(5839):807–810.
39. Conboy IM, Rando TA. Aging, stem cells and tissue regeneration: lessons from muscle. *Cell Cycle*. 2005;4(3):407–410.
40. Jofre-Monseny L, et al. Effects of apoE genotype on macrophage inflammation and heme oxygenase-1 expression. *Biochem Biophys Res Commun*. 2007;357(1):319–324.
41. Finch CE, Morgan TE. Systemic inflammation, infection, ApoE alleles, and Alzheimer disease: a position paper. *Curr Alzheimer Res*. 2007;4(2):185–189.
42. Couffinhal T, et al. Impaired collateral vessel development associated with reduced expression of vascular endothelial growth factor in ApoE-/- mice. *Circulation*. 1999;99(24):3188–3198.
43. Silva EA, Mooney DJ. Effects of VEGF temporal and spatial presentation on angiogenesis. *Biomaterials*. 2010;31(6):1235–1241.
44. Rattazzi M, et al. Calcification of advanced atherosclerotic lesions in the innominate arteries of ApoE-deficient mice: potential role of chondrocyte-like cells. *Arterioscler Thromb Vasc Biol*. 2005;25(7):1420–1425.
45. Qiao JH, Fishbein MC, Demer LL, Lusis AJ. Genetic determination of cartilaginous metaplasia in mouse aorta. *Arterioscler Thromb Vasc Biol*. 1995;15(12):2265–2272.
46. Zhang SH, Reddick RL, Burkey B, Maeda N. Diet-induced atherosclerosis in mice heterozygous and homozygous for apolipoprotein E gene disruption. *J Clin Invest*. 1994;94(3):937–945.
47. Hoe HS, Pocivavsek A, Dai H, Chakraborty G, Harris DC, Rebeck GW. Effects of apoE on neuronal signaling and APP processing in rodent brain. *Brain Res*. 2006;1112(1):70–79.
48. Trommsdorff M, et al. Reeler/Disabled-like disruption of neuronal migration in knockout mice lacking the VLDL receptor and ApoE receptor 2. *Cell*. 1999;97(6):689–701.
49. Vi L, et al. Macrophages promote osteoblastic differentiation in-vivo: implications in fracture repair and bone homeostasis. *J Bone Miner Res*. 2015;30(6):1090–1102.
50. Denoble AE, et al. Uric acid is a danger signal of increasing risk for osteoarthritis through inflammasome activation. *Proc Natl Acad Sci USA*. 2011;108(5):2088–2093.
51. Miller RA, Nadon NL. Principles of animal use for gerontological research. *J Gerontol A Biol Sci Med Sci*. 2000;55(3):B117–B123.